On the Relationship between African Easterly Waves and the African Easterly Jet

Stephanie Leroux, Nicholas M. J. Hall

On the Relationship between African Easterly Waves and the African Easterly Jet

STEPHANIE LEROUX

LTHE, Université de Grenoble, Grenoble, France

NICHOLAS M. J. HALL

LEGOS, Université de Toulouse, Toulouse, France

(Manuscript received 10 October 2008, in final form 5 February 2009)

ABSTRACT

This idealized modeling study investigates how convectively triggered African easterly waves (AEWs) are influenced by the intraseasonal variability of the African easterly jet (AEJ). A set of 10-day averaged zonally varying basic states is constructed with the NCEP-2 reanalysis (1979–2006). A primitive equation model is used to simulate linear AEWs on each of these basic states using the same idealized convective heating localized over the Darfur mountains as an initial trigger. It is shown that the transient response depends strongly on the basic state. With the same trigger, many configurations of the AEJ fail to produce a wave disturbance, while others produce strong easterly wave structures. Necessary conditions for the development of strong waves can be characterized by a strong jet, a strong vertical shear, or a strong and extended potential vorticity reversal. In strong-wave cases the jet is extended to the south and west, and the jet core is aligned with the maximum of surface westerlies, maximizing the vertical shear. The pattern that is optimal for generating easterly waves also closely resembles the dominant mode of variation of the AEJ revealed by an empirical orthogonal function (EOF) analysis of the set of basic states.

1. Introduction

African easterly waves (AEWs) are a seasonal phenomenon that displays intermittence within the season and variability from one year to another. Recently there has been a renewal of interest in aspects of easterly wave dynamics including their growth mechanisms and energy sources (Hall et al. 2006; Hsieh and Cook 2007, 2005), their origin (Thorncroft et al. 2008, hereafter THK08), and their interaction with convection (Cornforth et al. 2009; Hsieh and Cook 2008; Nicholson et al. 2008). However, our developing understanding of AEWs has not yet reached a point where we have a satisfying explanation for their intermittence. Any such an explanation will undoubtedly combine considerations of the origin of AEWs and the environment in which they grow and propagate. In this study we explore some aspects of the new ''triggering hypothesis'' that has recently emerged (Hall et al. 2006; THK08) as an alternative to the traditional instability mechanism related to the African easterly jet (AEJ).

Many studies have focused on these African synoptic-scale perturbations since the 1970s and the Global Atmospheric Research Program (GARP) Atlantic Tropical Experiment (GATE) campaign (e.g., Burpee 1972; Reed et al. 1969). Motivations for a better understanding of easterly waves are strong because these waves are associated with modulation of convection and rainfall over West Africa (e.g., Duvel 1990; Fink and Reiner 2003; Kiladis et al. 2006) and with the genesis of tropical cyclones (e.g., Avila and Pasch 1992; Thorncroft and Hodges 2001). Burpee (1972) was the first to note a mid-tropospheric reversal in meridional potential vorticity (PV) gradient at the latitude of the African easterly jet, consistent with Charney and Stern's (1962) and Fjortoft's (1950) necessary conditions for instability of a zonal flow. Since then, it has generally been assumed that African easterly waves result from small random perturbations growing exponentially on the AEJ through a barotropic/baroclinic instability mechanism. This instability hypothesis appears to be supported by the results of several idealized modeling studies (e.g., Rennick 1976; Simmons

Corresponding author address: Stephanie Leroux, LTHE, BP 53, 38 041 Grenoble CEDEX 09, France.
E-mail: stephanie.leroux@hmg.inpg.fr

DOI: 10.1175/2009JAS2988.1

1977; Mass 1979; Thorncroft and Hoskins 1994a,b; Paradis et al. 1995; Thorncroft 1995; Grist et al. 2002) showing realistic easterly wave structures growing on various unstable zonally uniform jets. Hall et al. (2006) give a summary of the different zonal jets used as basic states in a range of previous perturbation studies.

In the same paper, dynamical mode calculations are carried out with a more realistic basic state [climatological mean for June–September 1968–98; National Centers for Environmental Prediction (NCEP)-1 reanalysis] that varies zonally and includes both surface westerlies and a meridional circulation. The modes that grow on this realistic three-dimensional jet show a structure very similar to the composite wave structure found by the same authors (Kiladis et al. 2006). However, the modes grow very slowly and can even be neutralized with a realistic amount of surface damping. Given the limited zonal extent of the AEJ (at most two wavelengths of AEWs), it is suggested that the jet alone is not able to generate easterly wave structures from small random perturbations. The authors stress the need for a finite-amplitude perturbation upstream that can trigger transient structures that may resemble normal modes. This led to a revisiting of Carlson's (1969) idea that strong convective events can play this triggering role, for which there is some recent evidence based on observations. Berry and Thorncroft (2005) show the case of a strong AEW that seems to be initiated by several mesoscale convective systems over the Darfur mountains. This particular region is also identified by Mekonnen et al. (2006) and Kiladis et al. (2006) as a preferred location for initiation of convection preceding easterly waves.

THK08 investigate the triggering of easterly waves by applying an initial and localized convective heating in the same dry primitive equation model as in Hall et al. (2006). Given this strong initial perturbation localized over the Darfur mountains (that is, upstream of the region of wave growth), transient AEW structures are shown to develop on the zonally varying jet. An investigation of the sensitivity of the triggered waves to the location of the initial perturbation confirms that AEWs are more efficiently triggered by heating close to the entrance of the jet. It is thus suggested that intermittence of observed easterly waves may be explained by the variability of convective activity in this area rather than purely by considerations of the jet structure.

However, the fact remains that even if AEWs are triggered by some convective events upstream, they still rely on the presence of the jet to support propagation and development. Horizontal and vertical wind shears are still their source of energy through barotropic and baroclinic conversions, even if actual instability of the jet is no longer posited as the initiation mechanism. The triggering experiments in THK08 are all performed about the same basic state provided by the climatological mean for June–September 1968–98 (NCEP-1 reanalyses). In this paper we explore the consequences of variations of the jet on shorter periods within the season. Because easterly waves propagate in about a week from the jet entrance to the jet exit, they are likely to be sensitive to its intraseasonal variability. If triggered at different moments within the season, they will grow on different jets, which in turn may influence their development differently. How does the intraseasonal variability of the jet influence the triggered waves? We approach this question with the same type of idealized experiments as in THK08, but here the AEWs are triggered on a range of different basic states, all of them perturbed with the same initial heating, always localized at the same place. We thus investigate the sensitivity of the transient AEW-like response to a set of various realistic three-dimensional jets.

The set of basic states is presented in section 2 with a short description of its variability. Our modeling approach is detailed in section 3. The ensuing range of different easterly wave responses is shown in section 4, and in section 5 some further analysis based on composite states is shown to try to account for the variations we see. Conclusions are given in section 6.

2. The set of basic states

Basic states have been prepared from daily NCEP-2 reanalysis data (Kanamitsu et al. 2002), spectrally analyzed at T31 and interpolated to give vorticity, divergence, and temperature on 10 equally spaced sigma levels. A time–height independent divergence correction has been applied as outlined by Hall (2000). These daily fields have then been averaged over consecutive periods of 10 or 11 days so that three basic states are computed per month for June, July, August, and September from 1979 to 2006. This provides 336 different basic states on which easterly waves will be triggered. The use of nonoverlapping periods is not indispensible for the purpose of generating a set of basic states, but it will be seen that it provides an adequate number of samples over the time period for which we have data. The choice of a 10-day averaging period was made to give a clear separation between the phenomenon of the wave and the jet upon which it propagates while at the same time retaining variations that might affect wave growth within the season from one wave event to the next.

Figure 1 shows the mean and variance of zonal wind at level of the jet ($\sigma = 0.65$) and near the surface ($\sigma = 0.95$) for the 336 basic states. The mean jet is similar to

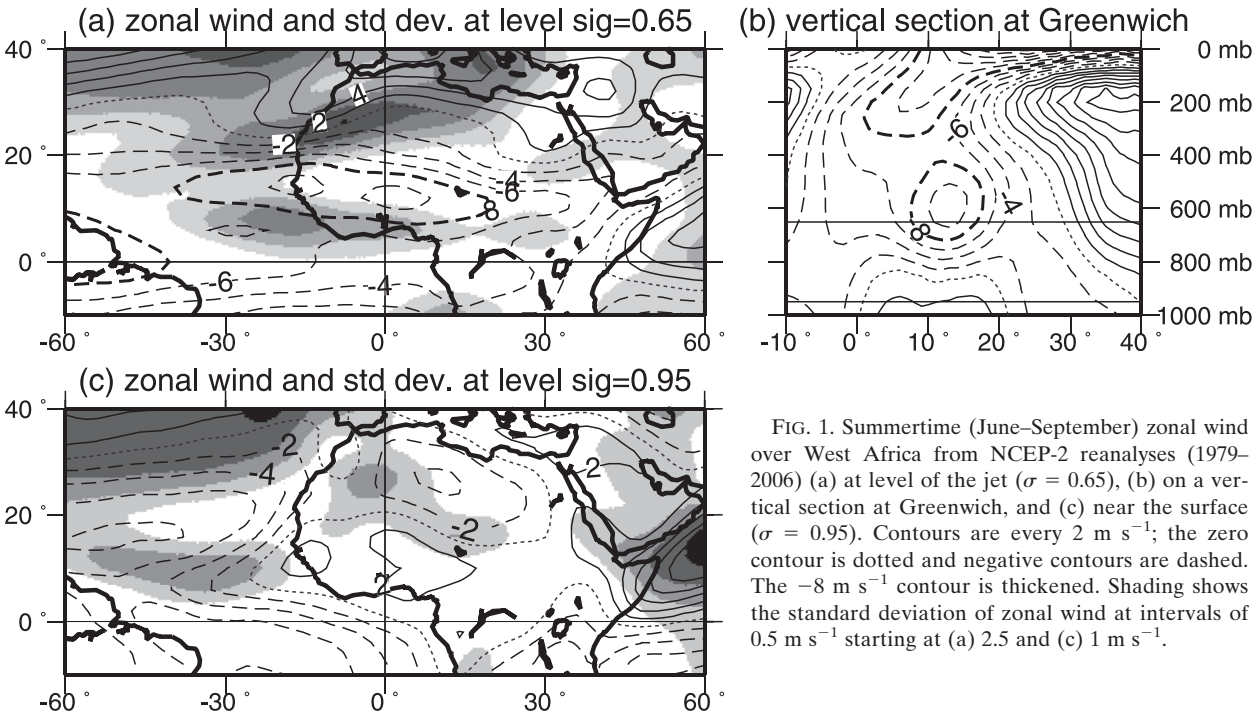

FIG. 1. Summertime (June–September) zonal wind over West Africa from NCEP-2 reanalyses (1979–2006) (a) at level of the jet (σ = 0.65), (b) on a vertical section at Greenwich, and (c) near the surface (σ = 0.95). Contours are every 2 m s^{-1}; the zero contour is dotted and negative contours are dashed. The −8 m s^{-1} contour is thickened. Shading shows the standard deviation of zonal wind at intervals of 0.5 m s^{-1} starting at (a) 2.5 and (c) 1 m s^{-1}.

the climatological jet from NCEP-1 reanalyses in THK08 but somewhat weaker, due mainly to a systematic difference between NCEP 1 and NCEP 2. The jet peaks around 12°N at about 600 mb with a maximum amplitude of 10 m s^{-1}. Maxima of standard deviation (around 4 m s^{-1}) appear on both flanks of the mean jet, but the core of the jet itself shows smaller variation (standard deviation lower than 2.5 m s^{-1}). At low levels, we note the presence of the surface westerlies of up to 2 m s^{-1} over the land between the Guinean coast and 20°N that reinforce the vertical wind shear below the AEJ.

Patterns of spatial variability for the 336 basic states have been constructed through a spatial empirical orthogonal function (EOF) analysis performed on the zonal wind at the level of the jet (σ = 0.65) and near the surface (σ = 0.95) in the region 5°–25°N, 45°E–45°W. The first and second EOFs obtained for both levels are presented in Fig. 2 (with standardized principal components PC1 and PC2 regressed against zonal wind at the same level for the whole set of basic states). They all pass the Scree and North tests (Cattell 1966; North et al. 1982).

At the level of the jet (σ = 0.65), the first EOF (Fig. 2a) explains 44% of zonal wind variance. It shows a strong north–south dipole pattern that indicates latitudinal variations of the jet at time scales greater than 10 days. The second EOF (Fig. 2b) explains 12% of the variance and describes longitudinal variations of zonal wind. These two EOFs are very similar to the patterns diagnosed in Leroux et al. (2009) using the daily NCEP-2 time series for the same period of the year (June–September). They calculate the EOFs with the unfiltered time series and also with seasonal cycle removed and with both seasonal cycle and synoptic activity removed. They show that the EOF patterns are not greatly changed by the time filtering and thus reflect both seasonal and intraseasonal variations.

At level σ = 0.95, the two main EOFs explain 34% and 20% of the variance, respectively. EOF1 (Fig. 2c) shows two main maxima: one located over the Atlantic around 8°N and the second over the continent at about 15°N, 15°E, with a positive minimum between them, around 10°N–0°. EOF2 (Fig. 2d) shows a land–sea (east–west) dipole.

3. Modeling approach

We carry out our perturbation experiments with the same model as in THK08. It is a global spectral primitive equation model with a horizontal resolution of T31 and 10 equally spaced sigma levels. A semi-implicit 22.5-min time step is used to integrate the full nonlinear equations for vorticity, divergence, temperature, and log(surface pressure). Because orography is not represented in the model, the surface pressure seen by the model is calculated from the 1000-mb geopotential height and 1000-mb temperature. A 12-h ∇^6 diffusion is applied to the momentum and temperature equation. Low-level damping is also applied as described in Hall

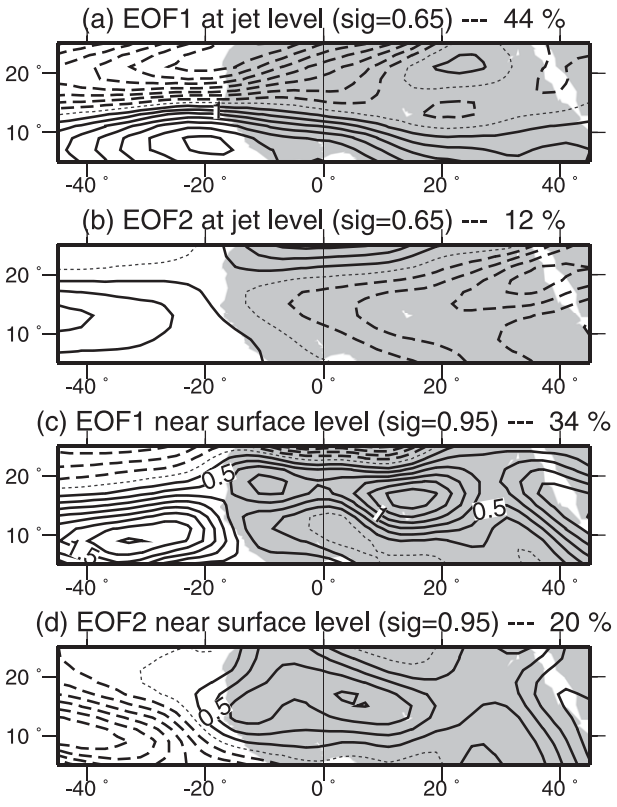

FIG. 2. First and second EOFs of zonal wind at (a),(b) the level of the jet (σ = 0.65) and (c),(d) near-surface level (σ = 0.95). These maps are projections of PC1 and PC2 onto the zonal wind field at same level for the whole set of basic states. Contours are every 0.5 m s^{-1} at level of the jet and every 0.25 m s^{-1} near surface level; the zero contour is dotted and negative contours are dashed. Percentages denote the variance explained.

et al. (2006) and THK08 to represent in a simple manner turbulent transfers of momentum and heat with the surface.

Each basic state is held constant by adding a different associated forcing term that compensates exactly for the development of the particular basic state when integrating the model for one time step without any initial perturbation [see Hall et al. (2006) for methodological details]. The perturbation experiment is then constrained to be linear by imposing a very small initial heating and subsequently rescaling the response for presentation and discussion.

As in THK08, we prescribe here an initial perturbation by adding a localized heating via the thermodynamic equation. It is applied for the first day of simulation and is then switched off. All the experiments carried out in the present study are perturbed with the same initial heating centered at 15°N, 20°E, just downstream of the Darfur mountains. It varies horizontally as

$$H = H_0 \cos^2\left(\frac{\pi}{2}\frac{r}{r_0}\right), \quad (1)$$

with a radius r_0 of 5°; H is set to zero for values of r greater than r_0. The vertical profile H_0 is the "deep convective" profile defined in THK08:

$$H_0 = \frac{\pi}{2}\sin(\pi\sigma), \quad (2)$$

with a vertically averaged value of H_0 of 5 K day^{-1}. In terms of latent heating, this would be equivalent to a peak precipitation at the center of 20 mm day^{-1}.

Our experimental setup has some features in common with the recent work of Nicholson et al. (2008); both use a primitive equation model with a selection of basic states taken from observations. However, there are several important differences. We use a zonally varying basic state in recognition of the fact that an AEW experiences changing conditions during its passage through the AEJ. Our trigger is baroclinic, as it comes from a hypothetical midtropospheric heating. And we consider many more basic states, concentrating on the large observed intraseasonal variability of the AEJ rather than on wet years and dry years.

In summary, we perform the same perturbation run on the 336 different basic states. Each basic state is maintained by the appropriate forcing and is perturbed for 1 day by the same initial heating applied at 15°N, 20°E. The model is integrated for 30 days to see the atmospheric response to this initial heating. We then compare the different transient responses triggered on the various basic states.

4. The set of wave responses

a. Four contrasting examples

We will first focus on four cases subjectively selected from the 336 triggering experiments to illustrate our modeling approach and the diversity of wave responses obtained. These contrasting examples underline the strong impact of the basic state on the triggered waves and reveal the complexity of the basic state–wave response relationship before more detailed investigations in the following sections.

As a starting point for comparison, we first show in Fig. 3 the run performed about our mean basic state (June–September 1979–2006, NCEP 2; Fig. 1). Maps of streamfunction anomaly at σ = 0.85 for the first, fifth, and ninth days of simulation illustrate the transient response of the atmosphere to the initial heating. At day 1 a trough has appeared. It moves westward, followed by a succession of ridges and troughs that form an AEW

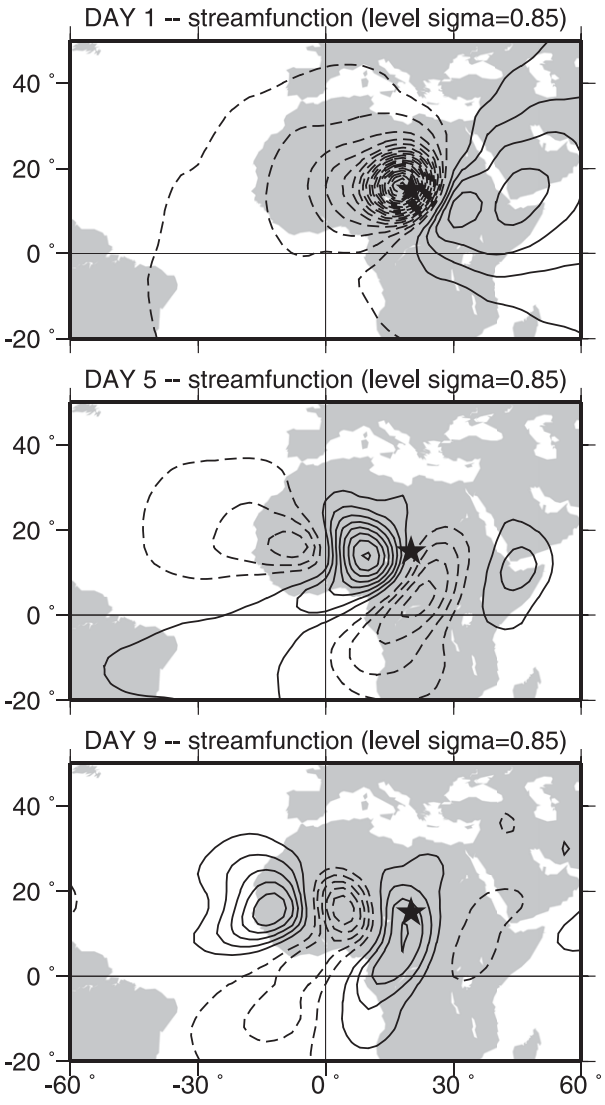

FIG. 3. Triggering experiment about the climatological June–September basic state for 1979–2006 (NCEP 2) comparable with the ''basic run'' performed in THK08 (see their Fig. 3). Streamfunction anomaly at $\sigma = 0.85$ for the first, fifth, and ninth days of simulation: contours are every 10^5 m^2 s^{-1}, with negative contours dashed (cyclonic circulations). The star represents the center of the initial heating perturbation.

structure (days 5 and 9). We note that it is a rather weak response compared with the response in the equivalent run in THK08 (see their Fig. 3): at day 9, their root-mean-square streamfunction anomaly at $\sigma = 0.85$ over the area 5°–25°N, 45°W–45°E is twice as strong as ours. However, as already pointed out in section 2, their climatological June–September basic state (1968–98) from NCEP 1 is different from our NCEP-2 basic state and this may explain the difference between the two responses.

The left panels of Fig. 4 present four contrasting examples from our set of 10-day-averaged basic states. Zonal wind is plotted at level $\sigma = 0.65$ and on a vertical section at Greenwich. The four AEJs are located between 10°N and 15°N, at about 600 hPa. The jets in examples 1 and 2 are weaker and narrower than jets 3 and 4, with peak zonal wind of about 12 m s^{-1}. Jet 2 is located further south than jet 1. Jets 3 and 4 peak at about 14 m s^{-1} but are centered on different longitudes: jet 3 peaks near the Atlantic coast whereas jet 4 peaks at the Greenwich meridian. In the vertical sections at Greenwich (central panels), the surface westerlies also vary significantly. They are almost nonexistent in example 4 but peak at about 4 m s^{-1} in example 3 and at 2 m s^{-1} in examples 1 and 2.

These four basic states were all perturbed with the same initial heating (applied for the first day of simulation and then switched off). The right panels of Fig. 4 show the transient responses (streamfunction anomaly at $\sigma = 0.85$) at day 9. As with the run about the mean basic state, by day 9 a succession of AEW-like ridges and troughs has formed. However, the four responses have very different amplitudes. Using the root-mean-square streamfunction anomaly at $\sigma = 0.85$ in the box 5°–25°N, 45°W–45°E as a measure of wave amplitude at day 9, we find that the waves in example 4 have an amplitude close to the amplitude of the waves in the run about the climatological basic state (Fig. 3). The waves triggered on basic states 2 and 3 are clearly stronger (respectively 2 and 4 times stronger at day 9 than the waves in the climatological run). The waves triggered on basic state 1 are 2 times weaker than in the climatological run.

The response to the initial heating is clearly influenced by the basic state. However, no obvious relationship between the basic state and the magnitude of the response emerges from these few examples. For instance, it is interesting to note that the magnitude of the response does not show a simple dependence on the jet strength. At least, there are striking counterexamples. Jets 3 and 4 both peak at about 14 m s^{-1} but jet 4 leads to a weaker wave response. On the contrary, jet 2 peaks at about 12 m s^{-1} like jet 1, but it leads to stronger waves. This does not mean that the jet strength has no impact at all on the response; it only suggests the complexity of the relationship. Some other factors must be involved in determining the intensity of the response and will be explored in the following sections.

b. *Statistics from the entire range of basic states*

We now use the whole set of 336 experiments to describe more systematically how the wave response varies. As an indicator of wave magnitude at a given day for a given simulation, we compute $\mathrm{wm}_{\mathrm{daily}}$, the root-mean-square streamfunction anomaly at $\sigma = 0.85$ over the

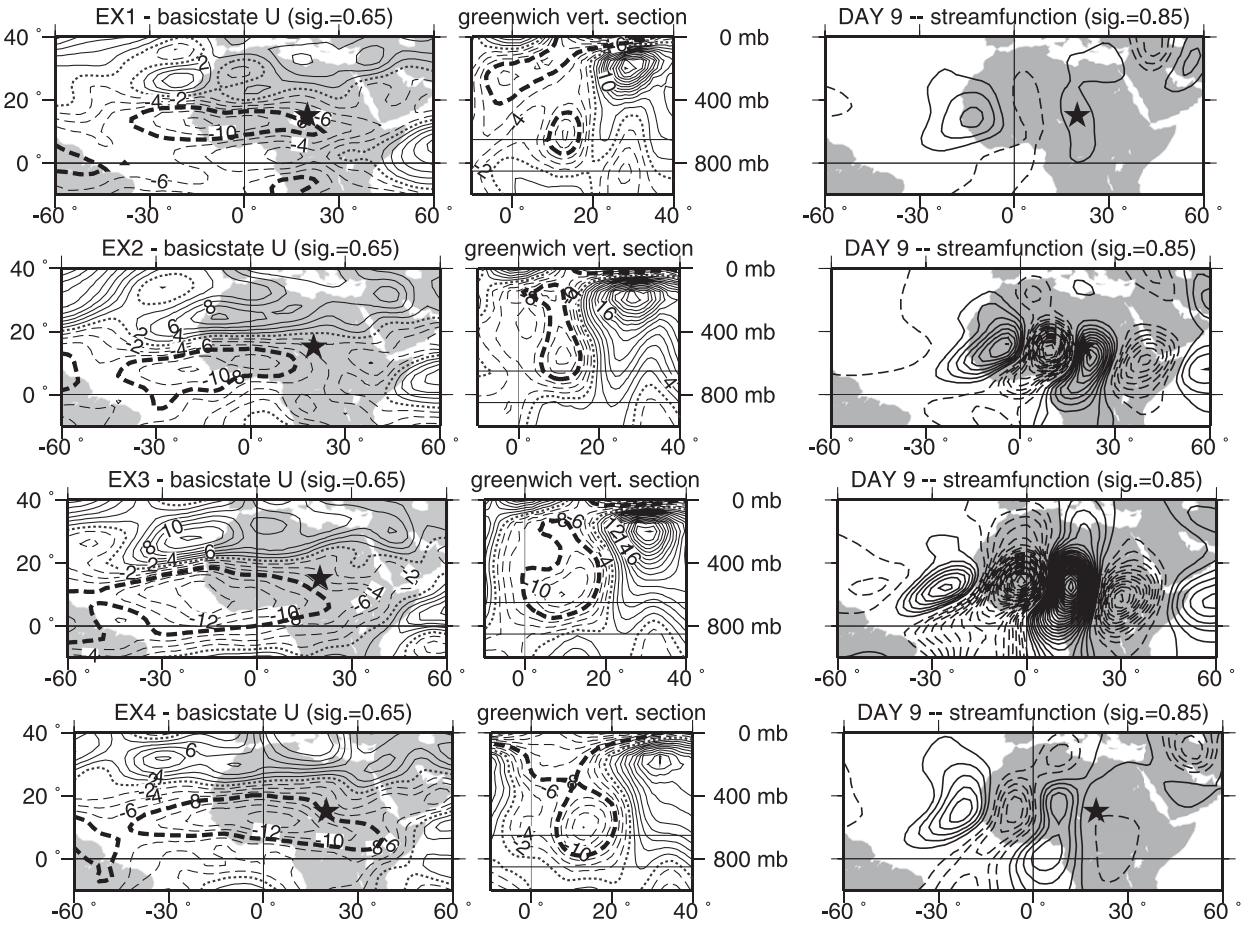

FIG. 4. Four examples of triggering experiments on 10-day averaged basic states (ex1, ex2, ex3, ex4). Basic state zonal wind at level $\sigma = 0.65$ and on a vertical section at Greenwich; contours are every 2 m s^{-1}, with the zero contour dotted and negative contours dashed. The -8 m s^{-1} contour is thickened. Streamfunction anomaly at $\sigma = 0.85$ for the ninth day of simulation; contours are every 10^5 m^2 s^{-1}, with negative contours dashed (cyclonic circulations). The star represents the center of the initial heating perturbation.

area 5°–25°N, 45°W–45°E. Then we define a standardized ''response index'', RI_{std}, for each experiment:

$$RI_{std} = \frac{RI - RI_{mean}}{\sigma}, \tag{3}$$

where RI is the average value of wm_{daily} from day 1 to 11 for the given experiment; RI_{mean} is the mean value of RI over the 336 experiments and σ is its standard deviation.

The distribution of this response index RI_{std} is plotted in Fig. 5a. We use RI_{std} to sort the 336 experiments into three classes:

- the top 20% ''strongest'' cases (wave response greater than the 80th percentile),
- the bottom 20% ''weakest'' cases (wave response smaller than the 20th percentile), and
- ''intermediate'' cases in which the response is between the 20th and 80th percentiles.

By definition, RI_{std} is zero for the mean intensity of the 336 experiments. The ''weak'' and ''strong'' cases are defined, as stated above, in comparison to this mean. The run performed about the climatological basic state (Fig. 3) is very close to this mean ($RI_{std} = -0.12$). Example 4 ($RI_{std} = 0.20$) illustrates another intermediate case close to the mean. Example 3 ($RI_{std} = 4.61$) is one of the strongest responses. Example 2 ($RI_{std} = 1.57$) illustrates another strong case. The distribution of RI_{std} (Fig. 5a) is not symmetrical: there are more weak waves ($RI_{std} < 0$) than strong waves ($RI_{std} > 0$), with many examples of an AEJ that does not produce a clearly identifiable wave response. One third of the experiments led to waves with a RI_{std} lower than -0.5. Example 1 ($RI_{std} = -0.93$) belongs to this weakest set and it is clear from Fig. 4 that by day 9 no strong AEW has developed.

Figure 5b presents the evolution of wm_{daily} with time for the strong and weak sets of responses. The peak

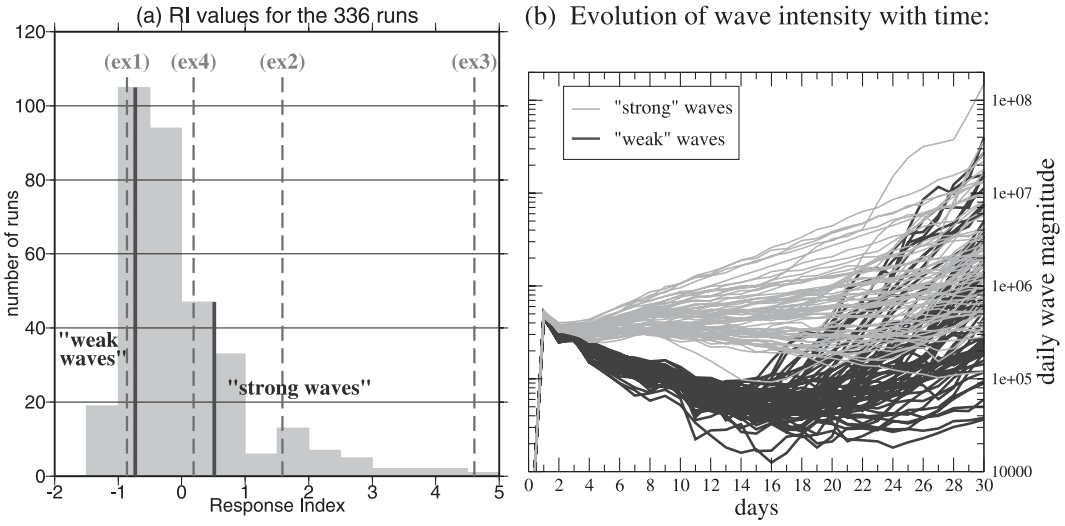

FIG. 5. (a) Distribution of the values of response index RI_{std} (see text) for the 336 experiments. Black lines separate the top 20% strongest wave cases (right end of histogram) and the bottom 20% weakest wave cases (left end of histogram). Ex1, ex2, ex3, and ex4 labels and gray dashed lines mark the values of RI_{std} for the four example runs of Fig. 4. (b) Evolution of wm_{daily} ($m^2\,s^{-1}$, log-scaled) with time for strong-wave (gray lines) and weak-wave cases (black lines).

value of wm_{daily} at day 1 reflects the formation of the first trough in response to the initial heating. After day 1 the heating is switched off. Note that even the strong responses do not always obtain values of wm_{daily} greater than that provided by the initial heating; they just succeed in converting it to easterly wave form. An examination of the daily streamfunction anomaly fields of the 336 runs (not presented here) shows that the exponential increase of wm_{daily} occurring after day 14 is not due to an AEW but rather is linked to unstable growth on the Asian jet in the model, which eventually influences the West African region. We therefore do not include the last part of the simulation in our analysis of the set of wave responses. As already said above, wm_{daily} values are averaged from days 1 to 11 only. As seen in Fig. 5b, 11 days gives enough time for an easterly wave life cycle.

We now proceed to investigate in more detail how the variability of the basic states is linked with the strength of the triggered wave response. At the level of the jet, a basic state with a negative PC1 means the easterly jet is stronger to the south over the Guinean coast, whereas a negative PC2 is related to the jet being stronger to the west over the Atlantic (see Figs. 2a,b). In Fig. 6, scatterplots are shown of the 336 experiments in PC1–PC2 space at the level of the jet (Fig. 6a) and near the surface (Fig. 6b). Black circles stand for the strongest wave cases, gray stars for the weakest wave cases, and small gray dots for intermediate cases. At level of the jet, strong- and weak-wave cases appear quite well separated. The two groups overlap but most of strong waves are clearly associated with negative values of PC1 and PC2, showing that strong waves are mainly associated with jets stronger in the south and west. At low levels, strong- and weak-wave cases also form two distinct groups. They are better separated along the x axis (low-level PC2) than along the y axis (low-level PC1). Most of the strong waves show positive values of low-level PC2, which implies a reinforcement of surface westerlies east of Greenwich at about 15°N (see Fig. 2d).

We note that the low-level EOFs are as efficient as the jet-level EOFs at separating strong- and weak-wave cases. We can separate strong- and weak-wave cases better by combining the EOFs from the two levels. Figure 7 shows a scatterplot of the 336 experiments in a new frame that combines indicators from $\sigma = 0.65$ and $\sigma = 0.95$. For the low level, we retain only $PC2_{\sigma=0.95}$ because it was the better separator in Fig. 6b; thus, $X = (PC2)_{\sigma=0.95}$ is used as the new x axis. For the jet level both PCs appear important, so we compute an indicator that is a combination of the two: $Y = 0.5(PC1 + PC2)_{\sigma=0.65}$. This is used as the new y axis. The patterns associated with variations in X and Y are shown in Fig. 7. The pattern in X is of course identical to $EOF2_{\sigma=0.95}$ presented in Fig. 2. The pattern in Y recovers the western part of the north–south dipole of $EOF1_{\sigma=0.65}$.

The two new axes X and Y are no longer necessarily orthogonal, and in fact the zonal wind at the two levels appears to be correlated. A northern and eastern AEJ tends to be associated with stronger low-level westerlies

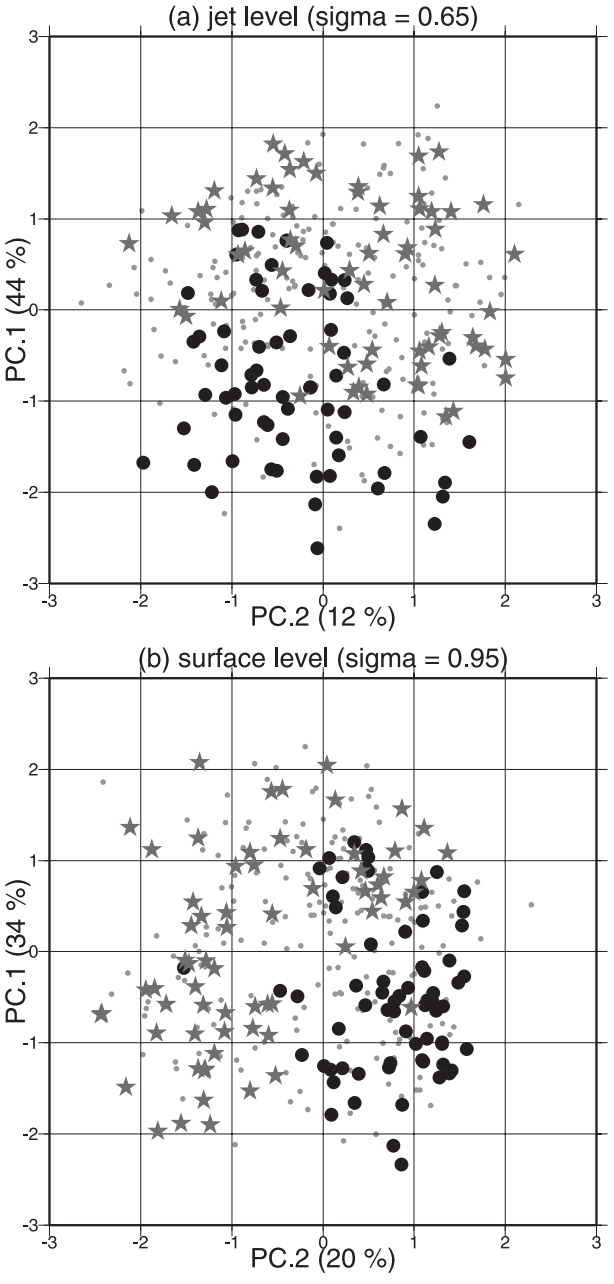

FIG. 6. Scatterplots of the 336 experiments as a function of PC1 and PC2 for zonal wind at (a) the level of the jet and (b) near the surface. Black circles denote the strong-wave cases, gray stars the weak-wave cases, and small gray dots intermediate cases. Percentages indicate how much zonal wind variance is explained by each EOF at each level.

to the south, whereas a southern and western AEJ tends to be associated with stronger low-level westerlies to the north, just below the jet. Because of this, the combined measure from the two levels can only bring a modest improvement to the separation between strong- and weak-wave cases. But it is interesting to note that strong-wave cases are less scattered than weak-wave cases. It appears that negative values of Y and positive values of X are necessary conditions to trigger strong waves, but they are not sufficient conditions because there are still some weak-wave cases in this part of the scatterplot.

5. Composite strong- and weak-wave cases

Composite basic states

To diagnose the characteristics of basic states that have led, on average, to strong waves or to weak waves, we compare in Fig. 8 the mean basic state (Fig. 8b) with the composite basic states for the bottom 20% weakest waves (Fig. 8a) and the top 20% strongest waves (Fig. 8c). These composite basic states are computed as the average of the individual basic states that have led to the top 20% strongest and bottom 20% weakest waves. The zonal wind is presented at the level of the jet ($\sigma = 0.65$) and on a vertical section at Greenwich. The vertical wind shear, computed as zonal wind at the surface ($\sigma = 0.95$) minus zonal wind at level of the jet ($\sigma = 0.65$), is also shown in the middle panels. Areas of negative meridional PV gradient on the isentropic surface 320 K are shaded in the left and middle panels.

The composite jet for the strongest waves peaks 2 m s^{-1} faster than the composite jet for the weakest waves. It is also wider because of a shift of its southern flank to the Guinean coast while the northern flank is still situated around 15°N. The strong-wave jet also extends farther west, beyond the Atlantic coast. The difference between the strong- and weak-wave composites at $\sigma = 0.65$ is plotted in the bottom line of Fig. 8. The north–south dipole (± 8 m s^{-1}) confirms that the jet is reinforced in the south and west in strong-wave cases. Note that this pattern is quite similar to the dipole pattern of the first EOF of zonal wind at same level (Fig. 2a). The triggered AEWs are thus seen to be sensitive to the dominant mode of variability in the AEJ.

The vertical wind shear is consistently greater in the strong-wave composite basic state, peaking at about 14 m s^{-1} in the same area as the jet maximum, whereas it is about 4 m s^{-1} less in the weak-wave composite. The intensity of the vertical shear is mainly attributable to the strength of the jet. This is also emphasized by the difference between strong- and weak-wave composites (bottom line, Fig. 8), which mainly reflects the north–south dipole above the Atlantic coast already discussed at $\sigma = 0.65$. However, looking at the vertical sections at Greenwich (right panels, Fig. 8), we also note that the maximum in surface westerlies is shifted to the Guinean coast in weak-wave cases. Thus, for weak-wave cases,

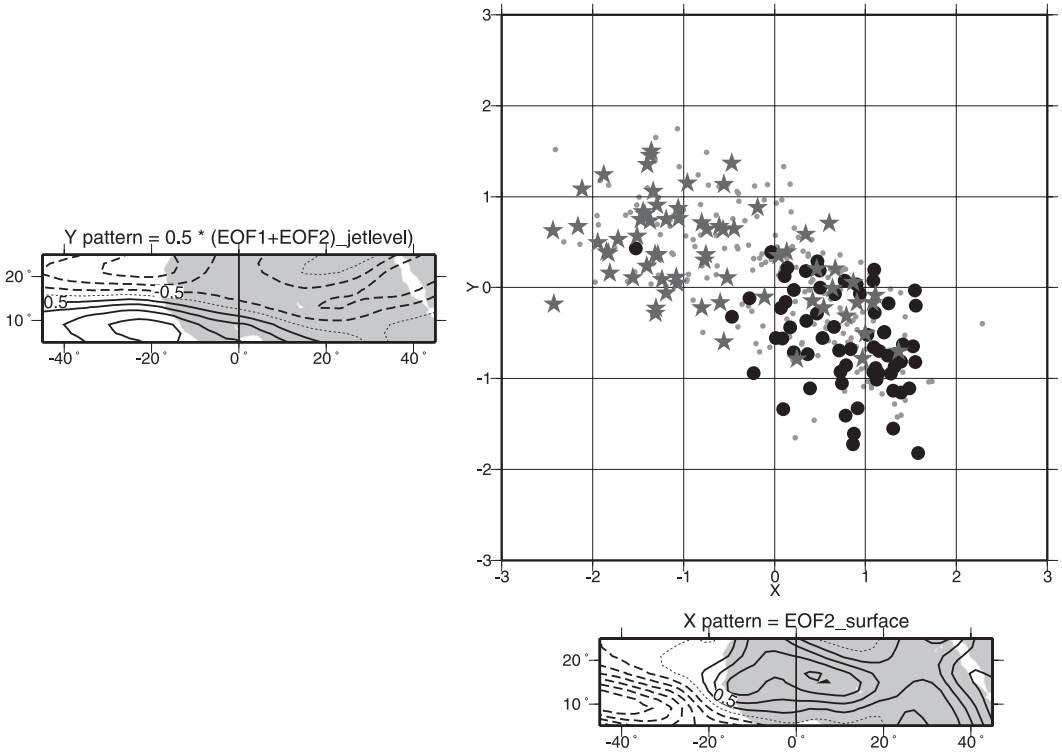

FIG. 7. Scatterplots of the 336 experiments as a function of $X = (\text{EOF2})_{\sigma=0.95}$ and $Y = (0.5)(\text{EOF1} + \text{EOF2})_{\sigma=0.65}$. Black circles denote the strong-wave cases, gray stars the weak-wave cases, and small gray dots intermediate cases. Regressions of zonal wind show the patterns corresponding to variations in X and Y. Contours are every 0.25 m s^{-1} near the surface level (X pattern) and every 0.5 m s^{-1} at level of the jet (Y pattern); the zero contour is dotted and negative contours are dashed.

there is a separation in latitude between the low-level westerlies and the narrow jet (15°N). In strong-wave cases, the maximum is located more to the north, around 15°N so it is aligned with the easterly jet. The surface westerlies may thus enhance the vertical shear by 1–2 m s^{-1} in the strong-wave configuration, where they align with the AEJ.

As shown in previous studies (e.g., Dickinson and Molinari 2000), a narrow strip of negative meridional PV gradient lies between 30°W and 30°E at about 15°N. This PV gradient reversal is more intense than the mean in cases that led to strong waves and less intense in cases that led to weak waves, but for both composites it is at the same latitude (about 15°N) on the northern flank of the jet and does not vary much in width. It should be remembered that the presence of a PV gradient reversal does not necessarily mean that the system is unstable. Hall et al. (2006) showed that such basic states can be stabilized by low-level damping, which is also applied in this study. On these stabilized basic states, AEWs need to be triggered by an initial perturbation. However, the PV gradient may serve as an indicator of the potential energy available for the transient perturbations to overcome dissipation for a limited time, rather than just as an instability criterion.

Figure 9 shows the life cycles based on the strong-wave and weak-wave composite basic states. The response based on the strong-wave composite is very similar in shape to the response about the mean basic state (already shown in Fig. 3), but the troughs and ridges are more intense (twice as strong at day 9 when computing the root-mean-square streamfunction anomaly at $\sigma = 0.85$ over the area 5°–25°N, 45°W–45°E). By day 9 we can see a slight difference in phase, with the stronger response being also slightly faster. The response about the weak-wave composite basic state is much smaller. At day 5 only one pair of faint vortices follows the initial trough and by day 9 the AEW has almost totally dissipated.

6. Discussion and conclusions

Our point of departure in this study has been the a priori assumption that African easterly waves need a finite-amplitude trigger. We have chosen a simulated convective trigger, as in THK08, and have used this

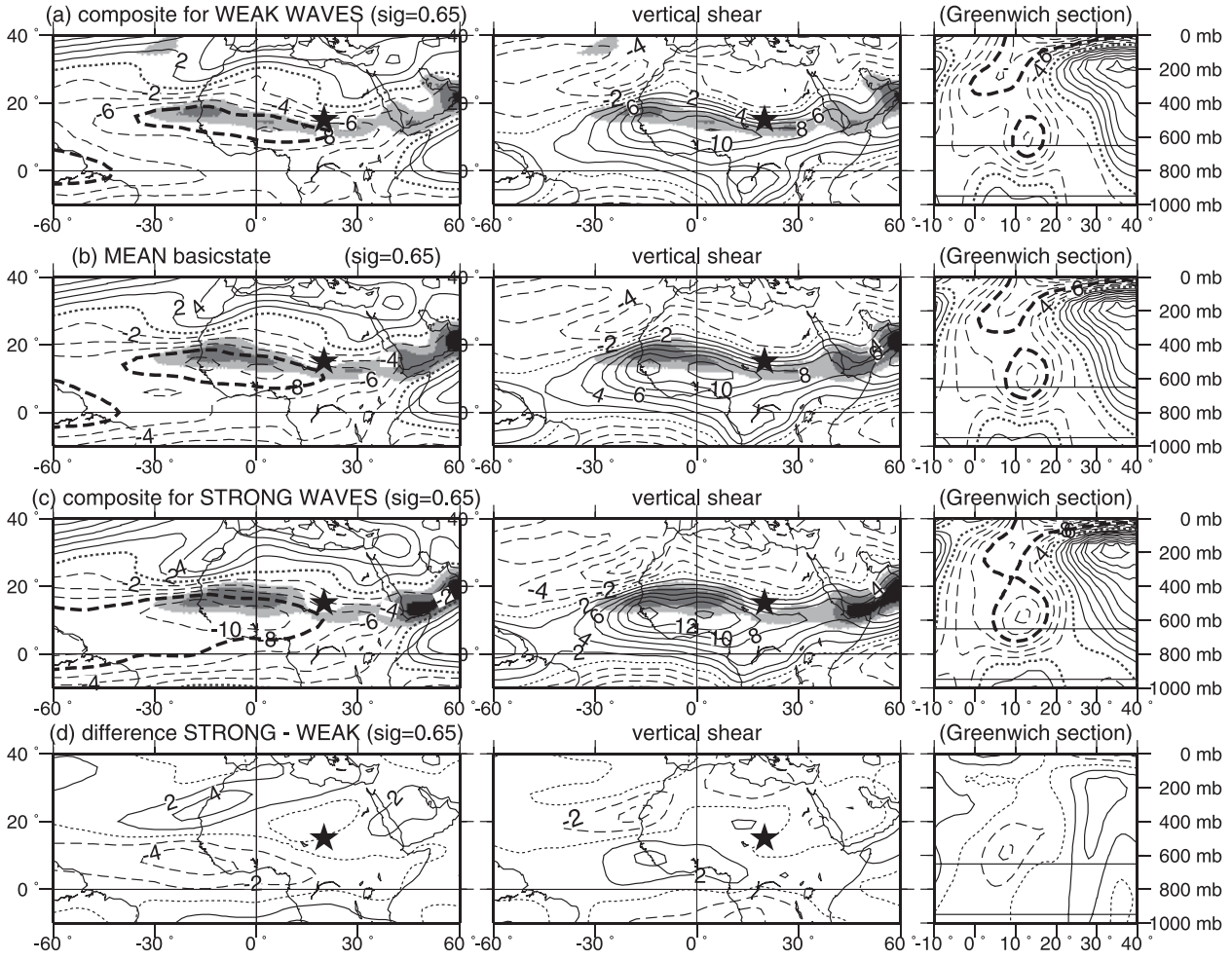

FIG. 8. Composite basic states for (a) the bottom 20% weakest waves and (c) the top 20% strongest waves; (b) the mean basic state; and (d) the difference (c) − (a). Contours are every 2 m s^{-1} for the zonal wind (left) at level $\sigma = 0.65$, (right) on a vertical section at Greenwich, and (center) for the vertical wind shear, taken between $\sigma = .95$ and the surface (also see text). The zero contour is dotted and negative contours are dashed. Dark shading represents the areas of negative meridional PV gradient at 320 K [at intervals of $0.005(10^{-6}$ K $m^{-1})$ kg^{-1} s^{-1} starting at -0.005]. The star represents the center of the initial heating perturbation.

experimental design to investigate the influence of a variable jet. Considering a large number of realistic three-dimensional basic states, it has been shown that the response to the convective trigger depends strongly on the basic state. With the same convective trigger, many configurations of the AEJ fail to produce a wave disturbance, whereas others produce strong easterly wave structures. This conclusion is based on a modeling approach in which a clear separation between cause and effect can be imposed, in this case by fixing the cause (convective heating), varying the passive environment (the basic state), and diagnosing the response.

The results show that the strength of the jet alone is not a sufficient indication of how strong the wave response will be. For a strong-wave response, the jet must be strong in the south and west, with near-surface westerlies underlying the core of the easterlies. This vertical alignment is clearly associated with greater vertical shear. This may be a key factor for transient wave growth, but it is not independent of the horizontal position of the jet, as the two factors are seen to covary within the sample of basic states used. The primary mode of natural variability reflected in the sample of basic states is a north–south dipole of zonal wind in the jet exit region (Fig. 2a). It is interesting to note that this pattern is almost identical to the pattern associated with variations in the strength of the wave response (Fig. 8d). This result was not built into the experiment a priori. It shows that the way in which AEWs respond dynamically to a convective heat source is conditioned by real observed variations in the AEJ.

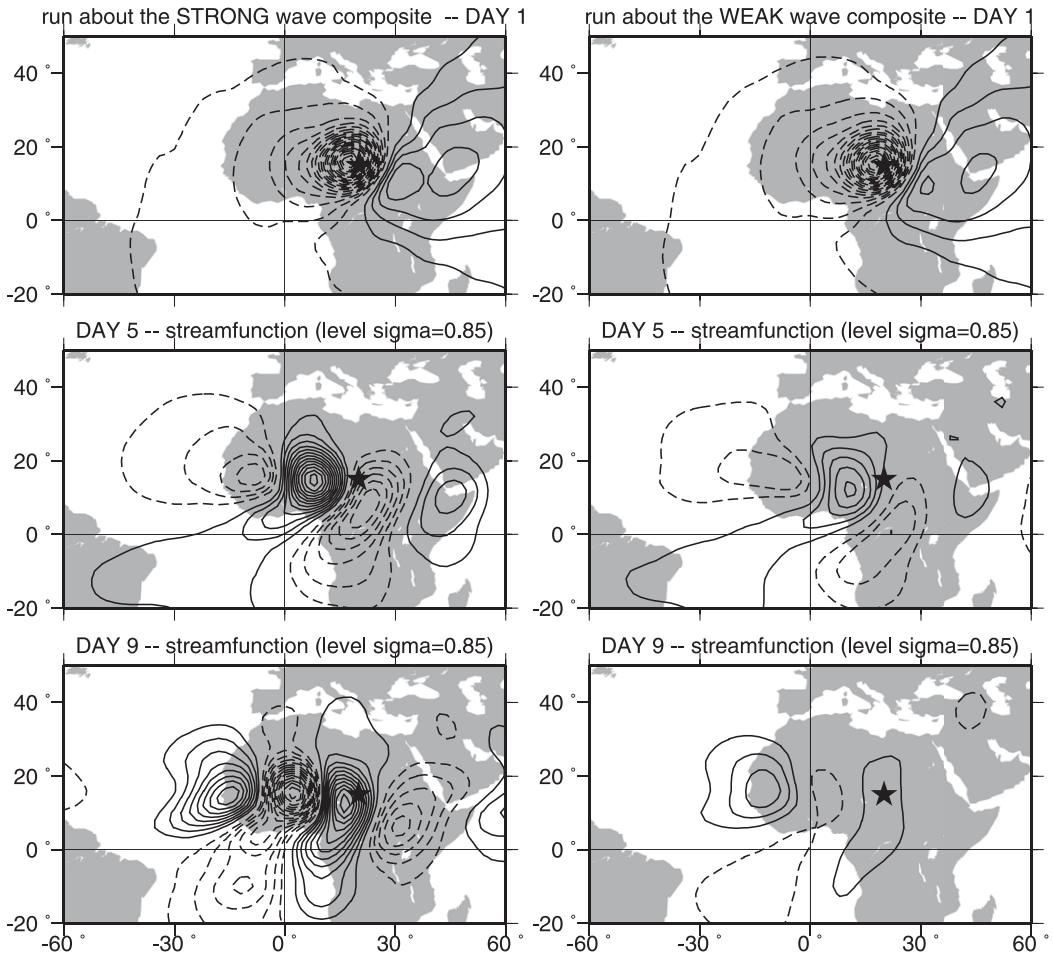

FIG. 9. Triggering experiments about the (left) strong-wave and (right) weak-wave composite basic states. Streamfunction anomaly at $\sigma = 0.85$ for the first, fifth, and ninth days of simulation: contours are every 10^5 m^2 s^{-1}, with negative contours dashed (cyclonic circulations). The star represents the center of the initial heating perturbation.

Further experiments have been carried out using composite basic states based on examples that individually lead to strong or weak responses. ''Typical'' life cycles based on these composite basic states lead to correspondingly strong or weak easterly waves. In the strong-wave composite the meridional potential vorticity gradient on the northern flank of the jet is stronger. It is tempting to seek a single indicator of wave response based on simple dynamical arguments applied to the basic state. The strength of the PV reversal seems like a good candidate. Whether or not the basic state is unstable, the strength of the PV reversal is a measure of the vertical shear and of the potential for transfer of available potential energy to boost the growth (or attenuate the decay) of a baroclinic easterly wave.

However, returning to the original set of experiments, Fig. 10a shows a scatterplot of the three classes of wave response as a function of the jet strength and the strength of the PV gradient reversal. Here, the strong- and weak-wave cases taken individually do not present any clear behavior related to this dynamical indicator, even though a relationship seemed to exist, on average, when looking at the composite results. It is thus seen that this measure is not as clear as the measure based on objective analysis shown above, even though the underlying dynamical arguments may be sound. Figure 10b shows interestingly that a better indicator is obtained by using the surface area covered by the jet and the PV gradient reversal rather than their strength. On this scatterplot, strong- and weak-wave cases are much better separated than on Fig. 10a, with strong-wave cases associated with a larger jet and a larger PV gradient reversal. Again, the importance of the spatial configuration of the basic state is emphasized.

A reversal in PV-gradient is often put forward as evidence of baroclinic instability. It is appropriate at this

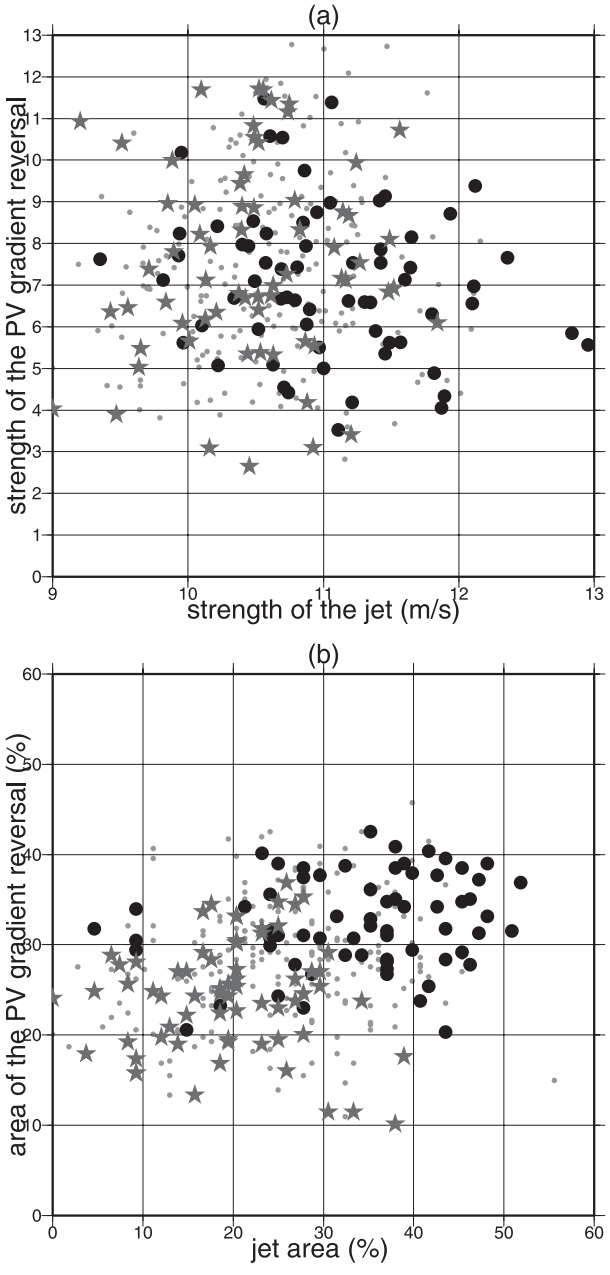

FIG. 10. (a) Scatterplot of the 336 experiments as a function of the strength of the PV gradient reversal [$-1000(10^{-6}$ K m^{-1} kg^{-1} s^{-1})] and the strength of the jet ("strength" computed as average in the area 5°–25°N, 45°W–20°E using only negative values of the PV gradient and only easterly wind stronger than 9 m s^{-1}). (b) Scatterplot of the 336 experiments as a function of the area covered by the PV reversal and by the jet (percentage of the area 5°–25°N, 45°W–20°E covered by negative values of PV gradient and by easterly wind stronger than 9 m s^{-1}). In both scatterplots, black circles denote the strong-wave cases, gray stars the weak-wave cases, and small gray dots intermediate cases.

point to discuss the relevance of this observation for the dynamics of AEWs. We argue in this paper, as previously in THK08 and Hall et al. (2006), that although the flow may be unstable, the system is stabilized by a modest amount of low-level damping. The mean AEJ is therefore part of a stable system and an isolated small perturbation will not grow into a large perturbation—hence the argument that a trigger is needed to initiate AEWs. The triggered waves still resemble the first normal mode of the system because this is still the most efficient structure for maintaining a disturbance against dissipation. But all the African waves shown in THK08 do eventually decay.

In the current study we must re-evaluate this position because we are no longer considering a climatological or seasonal basic state but rather a large population of basic states. Is it possible for some of them to be unstable enough to allow growth in the time available? This is easy to test, and normal-mode breeding experiments have been performed for the mean and composite jets studied here, with the same damping parameters. The mean state and the weak-wave state are stable. The strong-wave state is unstable. Its fastest-growing mode has easterly wave structure and a growth rate of 0.035 day^{-1}, so the *e*-folding time scale for normal modes on the strong-wave composite state is about a month. This is far too long to explain the intermittence of easterly waves as a result of jet variations with small perturbations. Recall that the jet variations we are considering are taken from 10-day averages and the wave disturbances themselves are even shorter lived. We conclude that although this study shows that variations in the AEJ are important to determine whether or not a given trigger event can produce an easterly wave, we still believe that the trigger event is necessary.

What emerges is a demonstration, in a simple modeling framework, that the convective trigger is necessary but not sufficient. A further necessary condition can be expressed either in terms of the structures of observed natural variability of the jet or in terms of dynamically relevant quantities such as vertical shear or PV gradient. Either way, as seen in the scatterplots in Figs. 6, 7, and 10, the strong-wave cases tend to be more tightly clustered than the weak-wave cases. Weak-wave cases can even intrude into the area populated by strong-wave cases. This indicates that although the identification of further necessary conditions is instructive and perhaps even potentially useful for forecasting, further work is needed to identify a sufficient condition for the genesis of AEWs.

Our experiments are conducted with a geographically fixed convective trigger and a variable jet. This is the other way round from THK08, who used a fixed jet and varied the position of the trigger. They found that a

position on the right jet entrance was most effective for generating AEWs. However, separate experiments (not shown) show that the extreme variations in response found in this study cannot simply be explained in terms of the relative position of the jet and the trigger. In fact, the northern flank of the jet does not move very much, so the standard position for the trigger, over the Darfur mountains, is nearly always optimal. Other factors such as jet strength, southern extension, westward extension, and vertical shear are important independently of the relative positions of the trigger and the jet entrance. As mentioned above, stronger baroclinicity clearly plays a role, but aside from considerations of baroclinic conversions, we speculate that a jet that is stronger in the western, downstream region might be more favorable to wave development simply because in this case the perturbation is not rapidly advected downstream during the incipient development stage of the wave. To develop, a wave must remain within the baroclinic zone. This is consistent with the finding (Fig. 10) that it is more beneficial to have a strong baroclinic zone spread on a wide area than to have a smaller region of intense baroclinicity.

In summary, our current hypothesis for the genesis and development of AEWs is as follows:

1) The system is stable, or weakly unstable, so a finite-amplitude trigger is required, as discussed in Hall et al. (2006).
2) The best position to trigger AEWs with a deep convective heat source is on the right entrance of the AEJ, in the Darfur region, as shown in THK08.
3) Intraseasonal variations in the AEJ determine whether or not a wave response can subsequently develop from the convective trigger. Necessary conditions for the development of a wave response can be characterized by strong shear or strong PV reversals over an extended region, and in addition to this we see stronger responses when the jet is extended to the south and west.

This vision of the initiation of AEW events is more selective than the one espoused in THK08, where the mere existence of a convective source was emphasized. It is also more stringent than the traditional view based on the state of the AEJ alone and the questionable instability argument that goes with it. In this paper we present a more comprehensive view in which two necessary conditions must be satisfied: a punctual trigger and a preconditioned basic state. This view is still not complete. To make further progress, the artificial separation of cause and effect in this study needs to be removed. In reality we expect a two-way interplay between the transients (AEWs) and the lower-frequency variations (the AEJ). Studies of observations and of unconstrained model runs need to be focused on clear questions about how the two components interact, including the feedback of AEWs on the AEJ. The relationship is likely to be complex and it will require a more thorough statistical approach to identify it. This is especially true if the intermittence of convective triggers turns out to be important. Observational aspects of the intermittence and genesis of AEWs and of their interplay with the AEJ are the subject of a subsequent contribution by Leroux et al. (2009).

Acknowledgments. We thank the two reviewers for their comments and suggestions, which greatly helped to improve the manuscript. Stephanie Leroux was supported by the French Ministry of ''Enseignement superieur et Recherche.'' This work is part of the AMMA project. AMMA (African Monsoon Multidisciplinary Analyses) was built by an international scientific group and is currently funded by a large number of agencies, especially from France, the UK, the U.S., and Africa. It has been the beneficiary of a major financial contribution from the European Community's Sixth Framework Research Programme. Detailed information on scientific coordination and funding is available on the AMMA International Web site (http://www.amma-international.org).

REFERENCES

Avila, L., and R. Pasch, 1992: Atlantic tropical systems of 1991. *Mon. Wea. Rev.,* **120,** 2688–2696.

Berry, G. J., and C. Thorncroft, 2005: Case study of an intense African easterly wave. *Mon. Wea. Rev.,* **133,** 752–766.

Burpee, R., 1972: The origin and structure of easterly waves in the lower troposphere of North Africa. *J. Atmos. Sci.,* **29,** 77–90.

Carlson, N., 1969: Synoptic histories of three African disturbances that developed into Atlantic hurricanes. *Mon. Wea. Rev.,* **97,** 256–276.

Cattell, R., 1966: The Scree test for the number of factors. *Multivariate Behav. Res.,* **1,** 245–276.

Charney, J., and M. Stern, 1962: On the stability of internal baroclinic jets in a rotating atmosphere. *J. Atmos. Sci.,* **19,** 159–172.

Cornforth, R. J., B. J. Hoskins, and C. D. Thorncroft, 2009: The impact of moist processes on the African easterly jet–African easterly wave system. *Quart. J. Roy. Meteor. Soc.,* **135,** 894–913.

Dickinson, M., and J. Molinari, 2000: Climatology of sign reversals of the meridional potential vorticity gradient over Africa and Australia. *Mon. Wea. Rev.,* **128,** 3890–3900.

Duvel, J.-P., 1990: Convection over tropical Africa and the Atlantic Ocean during northern summer. Part II: Modulation by easterly waves. *Mon. Wea. Rev.,* **118,** 1855–1868.

Fink, A. H., and A. Reiner, 2003: Spatiotemporal variability of the relation between African easterly waves and West African squall lines in 1998 and 1999. *J. Geophys. Res.,* **108,** 4332, doi:10.1029/2002JD002816.

Fjortoft, R., 1950: Application of integral theorems in deriving criteria for stability for laminar flows and for baroclinic circular vortex. *Geophys. Publ.,* **17,** 1–52.

Grist, J., S. Nicholson, and A. Barcilon, 2002: Easterly waves over Africa. Part II: Observed and modeled contrasts between wet and dry years. *Mon. Wea. Rev.,* **130,** 212–225.

Hall, N., 2000: A simple GCM based on dry dynamics and constant forcing. *J. Atmos. Sci.,* **57,** 1557–1572.

——, G. Kiladis, and C. Thorncroft, 2006: Three dimensional structure and dynamics of African easterly waves. Part II: Dynamical modes. *J. Atmos. Sci.,* **63,** 2231–2245.

Hsieh, J.-S., and K. H. Cook, 2005: Generation of African easterly wave disturbances: Relationship to the African easterly jet. *Mon. Wea. Rev.,* **133,** 1311–1327.

——, and ——, 2007: A study of the energetics of African easterly waves using a regional climate model. *J. Atmos. Sci.,* **64,** 421–440.

——, and ——, 2008: On the instability of the African easterly jet and the generation of African waves: Reversals of the potential vorticity gradient. *J. Atmos. Sci.,* **65,** 2130–2151.

Kanamitsu, M., W. Ebisuzaki, J. Woollen, S.-K. Yang, J. J. Hnilo, M. Fiorino, and G. L. Potter, 2002: NCEP–DOE AMIP-II Reanalysis (R-2). *Bull. Amer. Meteor. Soc.,* **83,** 1631–1643.

Kiladis, G., C. Thorncroft, and N. Hall, 2006: Three-dimensional structure and dynamics of African easterly waves. Part I: Observations. *J. Atmos. Sci.,* **63,** 2212–2230.

Leroux, S., N. Hall, and G. Kiladis, 2009: A climatological study of transient-mean flow interactions over West Africa. *Quart. J. Roy. Meteor. Soc.,* in press.

Mass, C., 1979: A linear primitive equation model of African wave disturbances. *J. Atmos. Sci.,* **36,** 2075–2092.

Mekonnen, A., C. D. Thorncroft, and A. R. Aiyyer, 2006: Analysis of convection and its association with African easterly waves. *J. Climate,* **19,** 5405–5421.

Nicholson, S. E., A. I. Barcilon, and M. Challa, 2008: An analysis of West African dynamics using a linearized GCM. *J. Atmos. Sci.,* **65,** 1182–1203.

North, G. R., T. L. Bell, R. F. Cahalan, and F. J. Moeng, 1982: Sampling errors in the estimation of empirical orthogonal functions. *Mon. Wea. Rev.,* **110,** 699–706.

Paradis, D., J.-P. Lafore, J.-L. Redelsperger, and V. Balaji, 1995: African easterly waves and convection. Part I: Linear simulations. *J. Atmos. Sci.,* **52,** 1657–1679.

Reed, R., D. Norquist, and E. Recker, 1977: The structure and properties of African wave disturbances as observed during Phase III of GATE. *Mon. Wea. Rev.,* **105,** 317–333.

Rennick, M., 1976: The generation of African waves. *J. Atmos. Sci.,* **33,** 1955–1969.

Simmons, A., 1977: A note on the instability of the African easterly jet. *J. Atmos. Sci.,* **34,** 1670–1674.

Thorncroft, C., 1995: An idealized study of African easterly waves. III: More realistic basic states. *Quart. J. Roy. Meteor. Soc.,* **121,** 1589–1614.

——, and B. Hoskins, 1994a: An idealized study of African easterly waves. I: A linear view. *Quart. J. Roy. Meteor. Soc.,* **120,** 953–982.

——, and ——, 1994b: An idealized study of African easterly waves. II: A nonlinear view. *Quart. J. Roy. Meteor. Soc.,* **120,** 983–1015.

——, and K. Hodges, 2001: African easterly wave variability and its relationship to Atlantic tropical cyclone activity. *J. Climate,* **14,** 1166–1179.

——, N. Hall, and G. Kiladis, 2008: Three dimensional structure and dynamics of African easterly waves. Part III: Genesis. *J. Atmos. Sci.,* **65,** 3596–3607.